A Synergistic Na-Mn-O Composite Cathodes for High-Capacity Na-Ion Storage

Xuanpeng Wang, Chenyang Wang, Kang Han, Chaojiang Niu, Jiashen Meng, Ping Hu, Xiaoming Xu, Zhaoyang Wang, Qi Li, Chunhua Han,* Yunhui Huang, and Liqiang Mai*

Searching for new-type cathodes to enhance the capacity of Na-ion batteries is one of the hot spots in energy storage systems. Many sodium insertion transition metal oxides, i.e., Na-Mn-O compounds, are intensively studied owing to their high voltage, abundant resources, and low toxicity. However, its relatively low capacity greatly limits its application. Here, a new synergistic composite, $0.44Na_4Mn_2O_5 \cdot 0.56Na_{0.7}MnO_2$, is developed by a feasible method of organic-acid-assisted drying and heat treatment. This synergistic composite cathode delivers a reversible sodium storage capacity as high as 278.0 mAh g^{-1} and stable framework structure due to the synergistic effect. It is achieved by the synergistic effect of high capacity $Na_4Mn_2O_5$ with multiple Na$^+$ ions insert/extract sites and stable $Na_{0.7}MnO_2$ with layered structure. Even when tested at a high mass loading of 7.42 mg cm^{-2}, this composite cathode demonstrates stable cycling over 400 cycles for sodium storage. Moreover, when coupled with hard carbon anode, Na-ion full battery delivers excellent charge/discharge performance with capacity retention of 84.0%, showing great application potential in the large-scale energy storage field.

1. Introduction

Na-ion batteries (NIBs) have been widely studied as one of the most promising candidates competitive with Li-ion batteries (LIBs) for large-scale energy storage systems.[1–7] Even if the raw materials of NIBs are cheaper, the energy-normalized cost of

NIB cells could reach \$0.14 Wh^{-1}, higher than that of LIB cells (\$0.11 Wh^{-1}).[8–11] Therefore, to demonstrate the low-cost advantage of NIBs in energy normalization, development of high-capacity electrode materials is extremely urgent.[1,4,9] High capacity with long cycle life cathode material is of most importance for high-performance NIBs.[2,12] In the past four decades, many transition metal oxide cathodes have attracted much interest.[2] Among them, manganese-based intercalation oxides are promising alternatives due to their high working potential, comparatively stable framework, low cost, and being eco-friendly.[1–4] Especially, layered Na-Mn-O type materials have been widely investigated for NIB cathode owing to their high operating voltage, good rate capability, and cycling stability.[13,14] Layered $NaMnO_2$ compounds exhibit enhanced intercalation property, compared to their Li analogs. As a result, $NaMnO_2$ compounds can sustain Na extraction without phase transition process.[15–19] Bruce and co-workers reported a new-type structured β-$NaMnO_2$ polymorphs cathode for NIBs.[15] It exhibits a capacity of 190.0 mAh g^{-1}, along with superior rate capability and capacity retention. Goodenough and co-workers investigated a high output voltage layered P3 structure $Na_{0.6}(Li_{0.2}Mn_{0.8})O_2$ cathode, and demonstrated that the plateau fading significantly over 50 cycles was attributed to the irreversible O-2p bands and the formation of amorphous phases.[16] Single crystalline $Na_{0.44}MnO_2$ nanowires with an excellent cycling performance as a cathode in NIBs was developed by Cao et al.[17] In addition, the layered α-Na_xMnO_2 and P2-$Na_{0.67}MnO_2$ compounds have also been systematically investigated as NIB cathodes.[18,19]

Despite all these favorable characteristics of layered $NaMnO_2$ compounds, the limited capacity cannot meet the high-energy density requirements.[16,20] Numerous studies have demonstrated that constructing P2 structured layered compound, partially substituting transition metal, and replacing alkali metal ions can improve the reversible sodium storage capacity of $NaMnO_2$ compounds.[21–26] A layered P2-$Na_{2/3}[Fe_{1/2}Mn_{1/2}]O_2$ is reported for the first time, and the layered cathode can deliver a reversible capacity of ≈190.0 mAh g^{-1} with an average voltage of 2.75 V versus Na$^+$/Na.[21] The energy density of the Na-ion cell is as high as ≈520 Wh kg^{-1}, which is close to $LiFePO_4$ in LIBs (530 Wh kg^{-1}). Cao and co-workers partially substituted Ni for

X. P. Wang, C. Y. Wang, K. Han, Dr. C. J. Niu, J. S. Meng, P. Hu, X. M. Xu, Z. Y. Wang, Dr. Q. Li, Dr. C. H. Han, Prof. L. Q. Mai
State Key Laboratory of Advanced Technology for Materials Synthesis and Processing
Wuhan University of Technology
Wuhan 430070, P. R. China
E-mail: hch5927@whut.edu.cn; mlq518@whut.edu.cn
Prof. Y. H. Huang
State Key Laboratory of Materials Processing and Die and Mould Technology
School of Materials Science and Engineering
Huazhong University of Science and Technology
Wuhan 430074, P. R. China
Prof. Y. H. Huang
Dong Guan McNair New Power Co., Ltd.
Dong Guan 523000, Guangdong, P. R. China

The ORCID identification number(s) for the author(s) of this article can be found under https://doi.org/10.1002/aenm.201802180.

Fe atoms in $Na_{0.67}Mn_{0.65}Fe_{0.35}O_2$, which not only alleviates the Jahn–Teller distortion of Mn element, but also provides more reversible sodium storage capacity and good cycling performance.[27] In our previous work, the novel K-intercalated layered Fe/Mn-based cathode has been constructed, and demonstrated that it can provide more reversible sodium storage sites and superior cycling stability during the sodiation/desodiation processes.[28] Although the reversible capacity of some intercalation cathode materials in NIBs is as high as that of a lithium-manganese spinel in LIBs, it is worth noting that the energy density of NIBs based on layered cathode is still considerably low.[9] Hence, the exploration and development of high-capacity NIB cathode materials still have a long way to go. In 1980s, the orthorhombic $Na_4Mn_2O_5$ material with Fddd space group was first reported by Brachtel et al.[29] However, its electrochemical sodium storage performance has not been revealed. Besides, a novel electrochemically active material, $Li_4Mn_2O_5$, has been studied as a promising LIBs cathode, which shows an ultra-high discharge capacity of 355.0 mAh g^{-1}, corresponding to 3 Li$^+$ insertion.[30,31] Therefore, we hypothesize that the similar crystal structure of $Na_4Mn_2O_5$ can accommodate more Na$^+$ ion extraction/insertion so that it may provide higher reversible sodium storage capacity. Recently, many studies indicate that introduction of a synergistic effect between different phases to construct a new composite material is an important approach to enhance the performance of NIBs.[32–36] Layered $Na_{0.66}Li_{0.18}Mn_{0.71}Ni_{0.21}Co_{0.08}O_{2+\delta}$ composite (P2 and O3) structures to achieve excellent performance in NIBs is reported by Guo et al.[32] An advanced radially aligned hierarchical columnar structure with Ni-rich core and Mn-rich shell as a high-performance NIB cathode is reported by Hwang et al.[35]

Herein, we designed and synthesized a novel synergistic composite structured $xNa_4Mn_2O_5 \bullet (1-x)Na_{0.7}MnO_2$ cathode and systematically studied the sodium storage performance of composite materials with different compositions ($x = 0.58$, 0.44, and 0.39). On the basis of in situ X-ray diffraction (XRD) and systematic electrochemical analysis, the synergistic composite structured cathode shows a high reversible capacity, excellent cycling, and rate performance. The optimized $0.44Na_4Mn_2O_5 \bullet 0.56Na_{0.7}MnO_2$ exhibits a considerable initial discharge capacity of 228.0 mAh g^{-1} with an average voltage of ≈2.55 V versus Na$^+$/Na when investigated as a cathode for NIBs. Even at a high mass loading of 7.42 mg cm^{-2}, the $0.44Na_4Mn_2O_5 \bullet 0.56Na_{0.7}MnO_2$ can work stably for 400 times. Moreover, Na-ion full batteries based on $0.44Na_4Mn_2O_5 \bullet 0.56Na_{0.7}MnO_2$/hard carbon are assembled, manifesting over 200 cycles.

2. Results and Discussion

2.1. Structure Characterization

The synergistic composite structured $xNa_4Mn_2O_5 \bullet (1-x)Na_{0.7}MnO_2$ was synthesized through a facile organic-acid-assisted drying combined with high temperature sintering method. The crystal structure of the as-prepared sample was determined through XRD measurement, from which the sample was well indexed to the hybrid phase of $Na_4Mn_2O_5$ (JCPDS No. 01-070-0428) and $Na_{0.7}MnO_2$ (JCPDS No. 00-027-0752) (**Figure 1**A). The $Na_4Mn_2O_5$ crystalline structure possesses an orthorhombic symmetry and space group of Fddd, with cell parameters $a = 5.72$, $b = 9.42$, $c = 19.67$ Å. The Mn^{3+} shows the coordination number of 5 in case of a ternary oxide (MnO$_5$), demonstrating an ordered derivative-type structure (Figure S1, Supporting Information), first investigated by Brachtel et al.[29] Figure 1B shows a view of the refined crystal structure of $Na_4Mn_2O_5$ with the corner-sharing and edge-sharing MnO$_5$ quasi-tetrahedron layers stacked along the c axis. This phase exhibits a quasi-layered structure with Na$^+$ ions sandwiched between Mn-O slabs. The layered structure of $Na_{0.7}MnO_2$ can be assigned to orthorhombic crystal symmetry with a space group of Cmca, showing a highly stable crystal plane for Na$^+$ ions insertion/extraction (Figure S2, Supporting Information).[19]

The ratio of the two phases ($Na_4Mn_2O_5$ and $Na_{0.7}MnO_2$) in the final sintered products will change with the proportion of Na-source and Mn-source in the reaction. When the proportion of Na-source and Mn-source are 6:2, 4:2, and 2:2, the final sintered products are $0.58Na_4Mn_2O_5 \bullet 0.42Na_{0.7}MnO_2$,
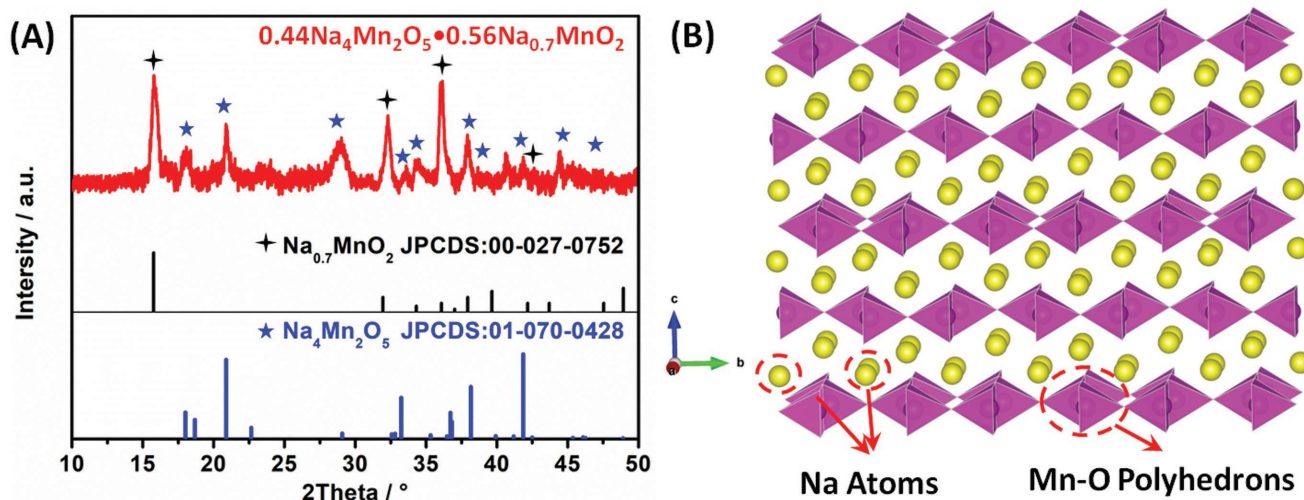
Figure 1. A) XRD patterns of $0.44Na_4Mn_2O_5 \bullet 0.56Na_{0.7}MnO_2$, B) the crystal structure of $Na_4Mn_2O_5$.

**ADVANCED
SCIENCE NEWS**
www.advancedsciencenews.com

**ADVANCED
ENERGY
MATERIALS**
www.advenergymat.de
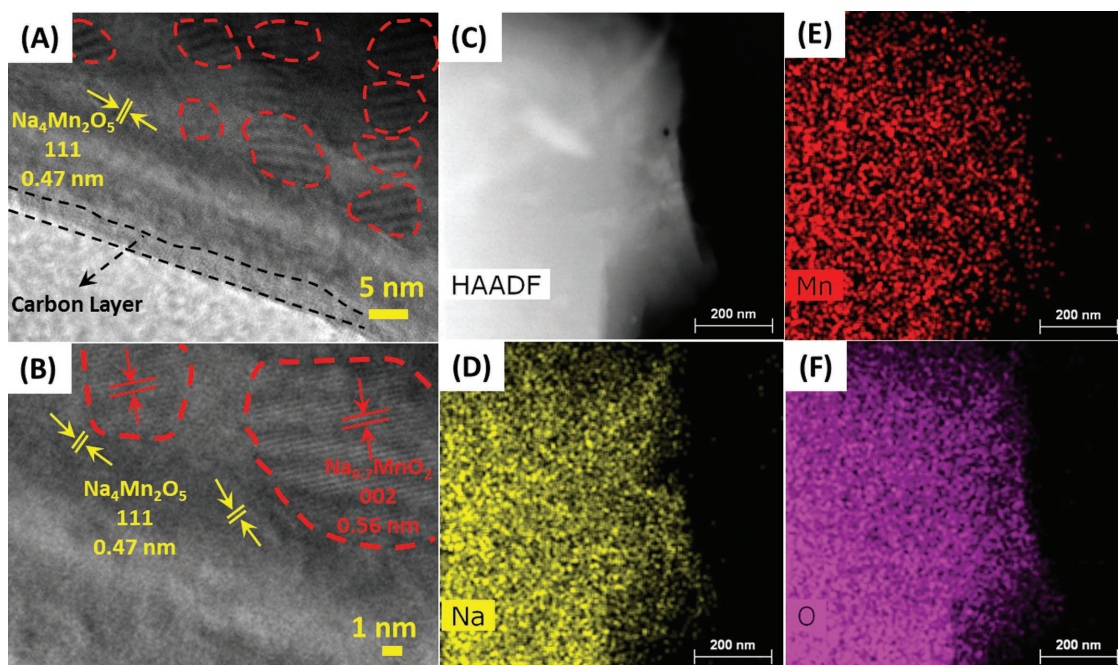
Figure 2. A) TEM image and B) high-resolution TEM (HRTEM) image, C–F) High angle annular dark field (HAADF) image and STEM-EDS elemental mappings of $0.44Na_4Mn_2O_5 \cdot 0.56Na_{0.7}MnO_2$.

$0.44Na_4Mn_2O_5 \cdot 0.56Na_{0.7}MnO_2$, and $0.39Na_4Mn_2O_5 \cdot 0.61Na_{0.7}MnO_2$ (Table S1, Supporting Information), respectively, based on the inductively coupled plasma (ICP) tests. XRD patterns of the three Na-Mn-O composite samples when sintered at 1100 °C clearly show highly crystalline phases and similar crystal diffraction peaks (Figure S3, Supporting Information). Scanning electron microscope (SEM) results show that the three Na-Mn-O composite samples have similar stepped morphologies (Figure S4A,D,G, Supporting Information). The stepped morphology may be shaped by the alternating crystallization of different phases.[37] Energy-dispersive X-ray spectroscopy (EDS) images show that Na, Mn, O, and C elements are uniformly distributed on each sample (Figure S4B,E,H, Supporting Information). The ratio of Na:Mn from EDS elemental analysis are 2.85:2.00, 2.51:2.00, and 2.39:2.00, respectively, which are in accordance with the ICP results (Figure S4C,F,I, Supporting Information). The high-resolution SEM images of the $0.44Na_4Mn_2O_5 \cdot 0.56Na_{0.7}MnO_2$ are presented in Figure S5 in the Supporting Information. Transmission electron microscope (TEM) was used to elucidate the detailed structure of the $0.44Na_4Mn_2O_5 \cdot 0.56Na_{0.7}MnO_2$ (**Figure 2**). Carbon layer with thickness of ≈2 nm is observed on the surfaces of the composite (Figure 2A). HRTEM images display that the lattice fringes of $Na_4Mn_2O_5$ and $Na_{0.7}MnO_2$ are ≈0.47 and ≈0.56 nm (Figure 2A,B), respectively. As shown in Figure 2C–F, the STEM-energy-dispersive spectroscopy (STEM-EDS) mapping images demonstrated uniform distribution of Na, Mn, and O elements, and were completely consistent with the selected image and SEM mapping results. Thermogravimetric analysis (TGA), Raman spectroscopy, and Fourier transform infrared spectroscopy (FT-IR) curves of $0.44Na_4Mn_2O_5 \cdot 0.56Na_{0.7}MnO_2$ are shown in Figures S6 and S7 in the Supporting Information. The carbon contents of the $0.44Na_4Mn_2O_5 \cdot 0.56Na_{0.7}MnO_2$

is determined to be ≈2.57%. For the sample, the peak intensity and position of the G-band is comparable to that of the D-band, manifesting the carbon is partially graphitized in $0.44Na_4Mn_2O_5 \cdot 0.56Na_{0.7}MnO_2$.[38,39]

2.2. Theoretical Capacity and In Situ XRD Analysis

To study the sodium storage mechanism of the synergistic composite structured $0.44Na_4Mn_2O_5 \cdot 0.56Na_{0.7}MnO_2$ in NIBs, the galvanostatic intermittent titration technique measurement (GITT) was conducted (**Figure 3**A). The theoretical capacities and corresponding transferred electron numbers of $Na_4Mn_2O_5$, $Na_{0.7}MnO_2$, and $0.44Na_4Mn_2O_5 \cdot 0.56Na_{0.7}MnO_2$ composite are provided in Figure 3B. Based on GITT test, the theoretical charge capacity of $0.44Na_4Mn_2O_5 \cdot 0.56Na_{0.7}MnO_2$ reaches to 299.0 mAh g^{-1} (corresponding to the extraction of ≈2.0 Na$^+$ ions per formula). The theoretical discharge capacity is as high as 278.0 mAh g^{-1}, corresponding to the ≈1.9 Na$^+$ ions insert into the host materials. Notably, one small discharge voltage plateau is located at ≈2.45 V, corresponding to ≈0.8 Na$^+$ ions insertion.

In order to reveal the intrinsic sodium storage mechanism and synergistic effect, we elucidated the time-resolved phase evolution for the initial three cycles of the $0.44Na_4Mn_2O_5 \cdot 0.56Na_{0.7}MnO_2$ by combining in situ XRD (**Figure 4**; Figure S8, Supporting Information). The peaks located at 15.7° and 29.1° belong to $Na_{0.7}MnO_2$ (002) and $Na_4Mn_2O_5$ (115) reflections, respectively, and all reflections are highly symmetrical. First, no distinct changes are observed for the $Na_{0.7}MnO_2$ (002) and $Na_4Mn_2O_5$ (115) reflections during the initial charging process, but when the voltage reaches 4.0 V, the two peaks instantly disappeared. Second, two new peaks appear and are fixed at 14.9° and 28.8° during the discharge process,
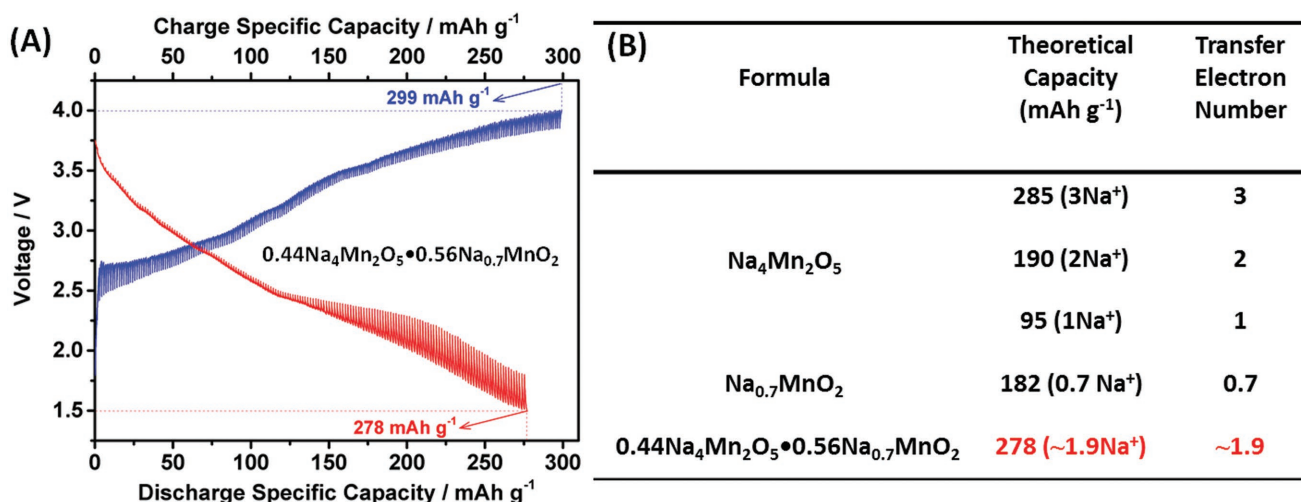
Figure 3. A) The GITT test for $0.44Na_4Mn_2O_5 \cdot 0.56Na_{0.7}MnO_2$ at 7.0 mA g^{-1}. B) The table of the theoretical capacities and correspondence transfer electron numbers.

Formula	Theoretical Capacity (mAh g^{-1})	Transfer Electron Number
	285 (3Na$^+$)	3
$Na_4Mn_2O_5$	190 (2Na$^+$)	2
	95 (1Na$^+$)	1
$Na_{0.7}MnO_2$	182 (0.7 Na$^+$)	0.7
$0.44Na_4Mn_2O_5 \cdot 0.56Na_{0.7}MnO_2$	278 (~1.9Na$^+$)	~1.9

and instantly disappeared at the end of the discharge process, respectively. Similar behavior also appeared in the following two cycles. Third, the other two peaks (20.8° and 36.7°) exhibit no obvious evolutions during cycling, indicating a stable intralayer Mn-O structure.[36,40,41] This trend is reversed during the desodiation/sodiation processes, showing a reversible crystal lattice expansion/contraction. The peak position of $Na_{0.7}MnO_2$ is restored to that of the initial position in the second cycle, manifesting a highly stable crystal structure. Moreover, the $Na_4Mn_2O_5$ (115) reflection also returned to its original position during the following cycles, confirming that $Na_4Mn_2O_5$ can deliver a stable quasi-layered crystal structure.[28,29,39,42,43]
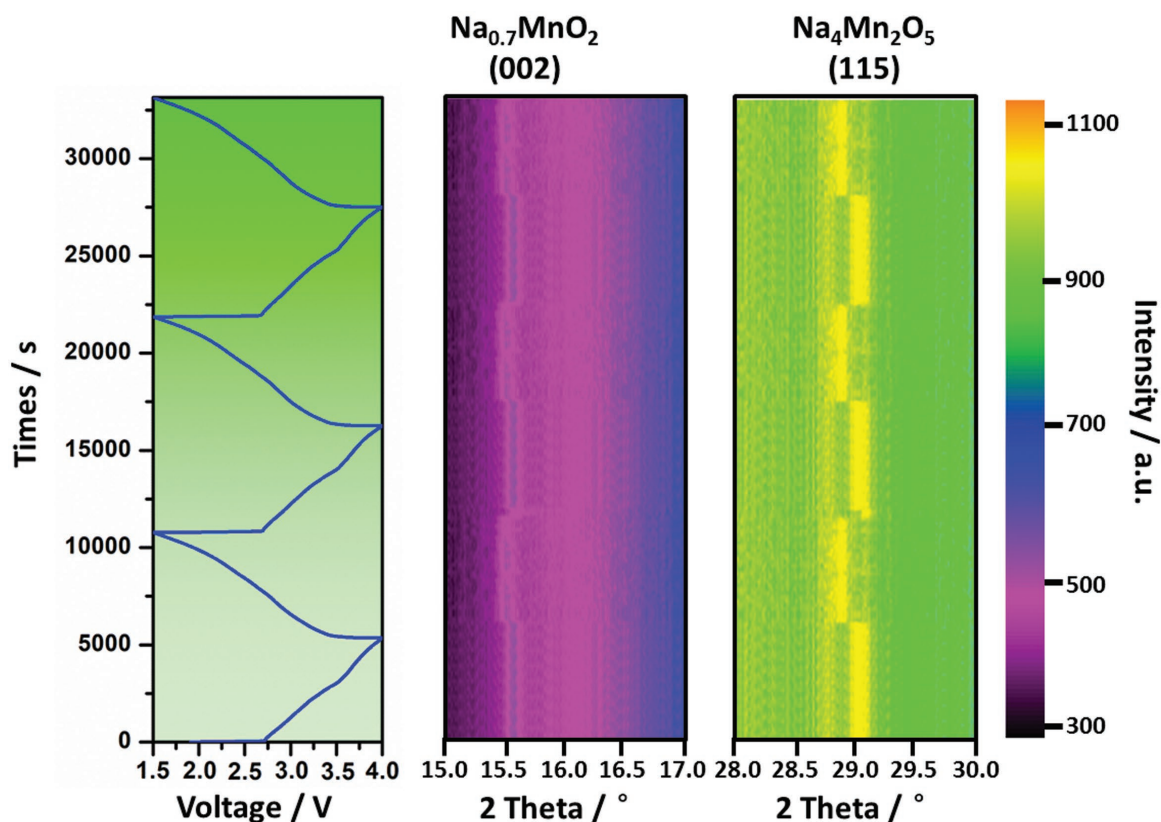
Figure 4. In situ XRD patterns of $0.44Na_4Mn_2O_5 \cdot 0.56Na_{0.7}MnO_2$ during galvanostatic charge/discharge at 150 mA g^{-1}. Image plots of XRD patterns at 15.0°–17.0° and 28.0°–30.0° during the initial three cycles.
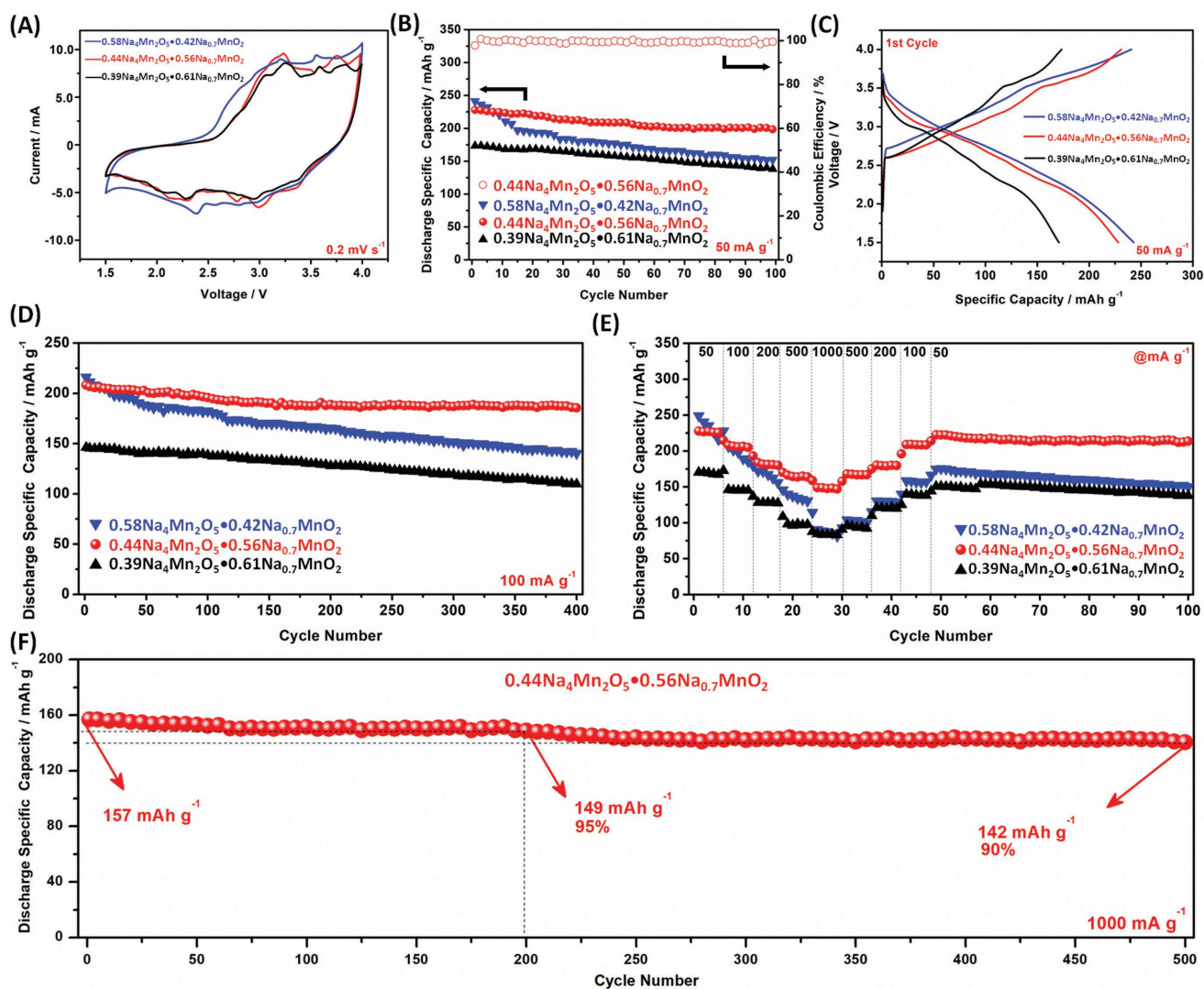
Figure 5. Electrochemical performance for xNa$_4$Mn$_2$O$_5$•$(1-x)$Na$_{0.7}$MnO$_2$ with mass loading of 3.89 mg cm^{-2} in half cell. A) Cyclic voltammograms. B) Cyclic performance and charge/discharge curves, C) tested at 50 mA g^{-1}. D) Cyclic performance at 100 mA g^{-1}. E) Rate performance. F) Long-life cycling performance measured at 1000 mA g^{-1}.

2.3. Electrochemical Performance in Half Cells

On the basis of the theoretical capacity calculation and in situ XRD characterization analysis, we confirm that Na$_4$Mn$_2$O$_5$ and Na$_{0.7}$MnO$_2$ can provide high reversible capacity and stable structure, respectively, during the Na$^+$ ions insertion/extraction processes. As a result, the 0.44Na$_4$Mn$_2$O$_5$•0.56Na$_{0.7}$MnO$_2$ composites exhibit excellent sodium storage performance when tested in NIBs. The synthesized three kinds of composites are tested as cathodes for NIBs (**Figure 5**; Figures S9–S11, Supporting Information). The cyclic voltammetry (CV) curves for three samples show similar hysteresis loop and some small cathodic/anodic peaks at a scan rate of 0.2 mV s^{-1} (Figure 5A). A pair of small reduction/oxidation peaks located at 3.55/3.45 V is assigned to Na$_{0.7}$MnO$_2$. Other peaks in the CV curves could be attributed to Na$_4$Mn$_2$O$_5$. Some small differences have also been observed for different samples. The reason of this phenomenon may be attributed to the presence of multiple Na$^+$ inserted

active sites in the Na-Mn-O composite, and some ruleless distortion sites at the grain boundary region between the two phases (Na$_4$Mn$_2$O$_5$ and Na$_{0.7}$MnO$_2$), resulting in different energies for Na$^+$ insertion/extraction and thus different positions of the redox peaks of the three composite materials.[36,43] To illustrate the reaction mechanism of 0.44Na$_4$Mn$_2$O$_5$•0.56Na$_{0.7}$MnO$_2$, we carried out ex situ X-ray photoelectron spectroscopy (XPS) tests to examine the evolutions in the oxidation states of Mn at different desodiation/sodiation states (Figure S9, Supporting Information). Based on the XPS test results, the high capacity results were obtained from the electrochemical activity of the Mn^{3+}/Mn^{4+} redox couples, both in Na$_4$Mn$_2$O$_5$ and Na$_{0.7}$MnO$_2$.[43,44] The cycling performances of the three composites are compared in Figure 5B–E. In general, the 0.44Na$_4$Mn$_2$O$_5$•0.56Na$_{0.7}$MnO$_2$ manifest best cycling stability and rate capability than other two composite samples. At a current density of 50 mA g^{-1}, the 0.44Na$_4$Mn$_2$O$_5$•0.56Na$_{0.7}$MnO$_2$ sample delivers an initial discharge capacity of 228.0 mAh g^{-1}

**ADVANCED
SCIENCE NEWS**

www.advancedsciencenews.com

**ADVANCED
ENERGY
MATERIALS**

www.advenergymat.de

with an average voltage of ≈2.55 V versus Na^+/Na, maintaining 199 mAh g^{-1} after 100 cycles (capacity retention of ≈87.0%). The theoretical energy density is approximately 580 Wh kg^{-1}, which is higher than that of $LiFePO_4$ (≈530 Wh kg^{-1} versus Li) and $LiMn_2O_4$ (≈450 Wh kg^{-1} versus Li). The initial coulombic efficiency (ICE) is as high as 97.6% and it stabilized at ≈99.5% after several cycles. The $0.39Na_4Mn_2O_5 \cdot 0.61Na_{0.7}MnO_2$ displays an initial capacity of 173.0 mAh g^{-1}, retaining 135.0 mAh g^{-1} after cycling 100 times (capacity retention of ≈78%) at the same current density. For $0.58Na_4Mn_2O_5 \cdot 0.42Na_{0.7}MnO_2$, the initial capacity can achieve 241.0 mAh g^{-1} at 50 mA g^{-1}, while only ≈62.0% of the initial discharge capacity is retained after 100 cycles (Figure 5B; Figure S10, Supporting Information). The initial charge/discharge curves of the three samples are presented in Figure 5C. Notably, the capacity retention of $0.44Na_4Mn_2O_5 \cdot 0.56Na_{0.7}MnO_2$ is 89.0% (small capacity fading of 0.028% per cycle) after cycling 400 times at current density of 100 mA g^{-1} (Figure 5D). By contrast, the $0.65Na_4Mn_2O_5 \cdot 0.35Na_{0.7}MnO_2$ and $0.58Na_4Mn_2O_5 \cdot 0.42Na_{0.7}MnO_2$ retain only 52.6% and 65.0% of their initial discharge capacities, respectively (Figure S11, Supporting Information). Notably, the $0.39Na_4Mn_2O_5 \cdot 0.61Na_{0.7}MnO_2$ and $0.27Na_4Mn_2O_5 \cdot 0.73Na_{0.7}MnO_2$ have high capacity retentions of 90.0% and 93.9%, respectively, showing excellent cycling stability. However, the two Na-Mn-O composites display low initial discharge capacities of 146.1 and 122.5 mAh g^{-1}, respectively (Table S2, Supporting Information). Therefore, the $Na_4Mn_2O_5$ phase plays the role on endowing the composite with high capacity, and the $Na_{0.7}MnO_2$ phase plays an important role on enhancing its cycling stability.

When tested at different current densities in rate measurements, $0.44Na_4Mn_2O_5 \cdot 0.56Na_{0.7}MnO_2$ delivers a considerable initial discharge capacity (227.0 mAh g^{-1}) and better capacity recovery (≈97.0%) than those of $0.58Na_4Mn_2O_5 \cdot 0.42Na_{0.7}MnO_2$ (249.0 mAh g^{-1}, ≈70.0%) and $0.39Na_4Mn_2O_5 \cdot 0.61Na_{0.7}MnO_2$ (170.0 mAh g^{-1}, ≈87.0%), manifesting the superior rate performance (Figure 5E; Figure S12, Supporting Information). When measured at 1000 mA g^{-1}, the $0.44Na_4Mn_2O_5 \cdot 0.56Na_{0.7}MnO_2$ exhibits an initial discharge capacity of 157.0 mAh g^{-1}, ≈95.0% of the initial capacity is retained after cycling 200 times, and it can stably operate for 500 cycles with a capacity retention of ≈90.0%, suggesting the prominent cycling stability (Figure 5F). As far as we know, the $0.44Na_4Mn_2O_5 \cdot 0.56Na_{0.7}MnO_2$ in this work exhibits the best electrochemical sodium storage performance among manganese-based cathode materials in terms of the reversible discharge capacity, cycling, and rate performance (Table S3, Supporting Information).[15,16,21,30,32,35,39,45]

A high mass loading is important for the cathodes to achieve high areal capacity in practice. Therefore, the electrochemical performance of $0.44Na_4Mn_2O_5 \cdot 0.56Na_{0.7}MnO_2$ at high mass loadings was investigated. Galvanostatic charge/discharge performance at 50 mA g^{-1} for high mass loading of 5.28 and 7.24 mg cm^{-2} was compared (**Figure 6**A,B). It was found that the $0.44Na_4Mn_2O_5 \cdot 0.56Na_{0.7}MnO_2$ delivered stable cycling performance at both mass loadings, with good capacity retention of 88.0% and 80.0% achieved at mass loadings of 5.28 and 7.42 mg cm^{-2} after 200 cycles, respectively. To further investigate the cycling stability of the composite (with high mass loading at 7.42 mg cm^{-2}) at high current density, cycling performance was measured at current density of 500 mA g^{-1}. After 100 cycles, good capacity retention of 86% was achieved (Figure 6C). Even for over 400 cycles, the stable cycling at mass loadings of 5.28 and 7.42 mg cm^{-2} with capacity retentions of 90% and 89% were also demonstrated, respectively (Figure 6D). Remarkably,
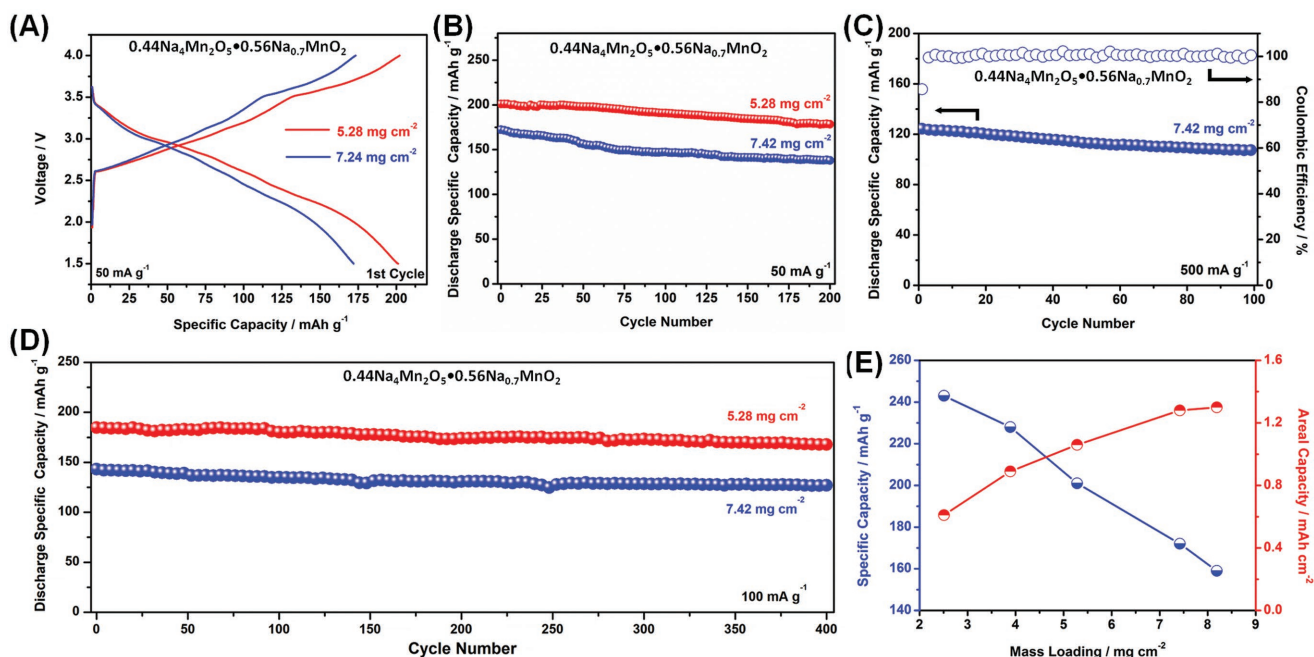
Figure 6. Electrochemical properties for $0.44Na_4Mn_2O_5 \cdot 0.56Na_{0.7}MnO_2$ with high mass loading. A) Desodiation/sodiation curves at different mass loadings. B) Cycling performance of $0.44Na_4Mn_2O_5 \cdot 0.56Na_{0.7}MnO_2$ at 50 mA g^{-1} with a mass loading of 5.28 and 7.42 mg cm^{-2}, respectively. C) Cyclic performance at 500 mA g^{-1}. D) Cycling performance of $0.44Na_4Mn_2O_5 \cdot 0.56Na_{0.7}MnO_2$ at 100 mA g^{-1} with mass loadings of 5.28 and 7.42 mg cm^{-2}, respectively. E) Specific capacities and areal capacities of $0.44Na_4Mn_2O_5 \cdot 0.56Na_{0.7}MnO_2$ at different mass loadings.

ADVANCED
SCIENCE NEWS
www.advancedsciencenews.com

ADVANCED
ENERGY
MATERIALS
www.advenergymat.de

as the mass loading increased from 2.51 to 8.19 mg cm^{-2}, the areal capacity increased from 0.61 to 1.30 mAh cm^{-2} (Figure 6E). The remarkable sodium storage performance of the $0.44Na_4Mn_2O_5 \cdot 0.56Na_{0.7}MnO_2$ can be attributed to its synergistic composite structure. These results proved that $0.44Na_4Mn_2O_5 \cdot 0.56Na_{0.7}MnO_2$ is a promising candidate for NIB cathodes.

2.4. Electrochemical Performance in Full Cells

The Na-ion full cells based on $0.44Na_4Mn_2O_5 \cdot 0.56Na_{0.7}MnO_2$ and hard carbon are also assembled. Before the full cells are fabricated, the SEM, TEM, XRD, Raman spectra, and electrochemical property characterizations of hard carbon are presented in Figures S13–S15 in the Supporting Information. **Figure 7**A displays the schematic of the Na$^+$ ion conduction between $0.44Na_4Mn_2O_5 \cdot 0.56Na_{0.7}MnO_2$ and hard carbon during the Na$^+$ ion insertion/extraction. The corresponding lighted LED screen shows that the Na-ion full cell can properly function when fully charged (Figure 7B). As shown in Figure 7C, the full cell displays an initial discharge capacity of 150 mAh g^{-1} (based on cathode) at 50 mA g^{-1}, retaining 129.0 mAh g^{-1} after cycling 100 times. The ICE is ≈88.0%, and the CE will increase to ≈98.0% in the following cycles (Figure 7C,D). When measured at a current density of 500 mA g^{-1}, ≈85% of the initial capacity can be maintained after 200 cycles (Figure 7E). As the current density increases from 30 to 500 mA g^{-1}, the full Na-ion cell shows an average capacity of 179.0, 149.0, 130.0, 113.0, and 100.0 mAh g^{-1}, respectively, demonstrating an excellent rate performance (Figure 7F). A good recovery

(≈97.0%) was observed when the current density gets back to 50 mA g^{-1}. These results indicate the good rate capability and cycling stability of $0.44Na_4Mn_2O_5 \cdot 0.56Na_{0.7}MnO_2$ in Na-ion full cells.

The remarkable sodium storage performance of the $0.44Na_4Mn_2O_5 \cdot 0.56Na_{0.7}MnO_2$ can be attributed to their synergistic composite structure. On one hand, the $Na_4Mn_2O_5$ possesses more sites for Na$^+$ ions insertion/extraction, resulting in high theoretical capacity (Figure 3A,B). On the other hand, the layered structure of $Na_{0.7}MnO_2$ can provide a stable framework, thus bringing on excellent cycling stability.[19] Combining with both advantages, the synergistic effect between high capacity $Na_4Mn_2O_5$ and ultra-stable layered $Na_{0.7}MnO_2$ results in superior sodium storage performance of $0.44Na_4Mn_2O_5 \cdot 0.56Na_{0.7}MnO_2$ (Figure 4). These achievements, including high specific capacity, high areal capacity, and stable cycling performance at high mass loadings of $Na_4Mn_2O_5 \cdot Na_{0.7}MnO_2$ as NIB cathodes, are highly significant for the innovation of Na-ion full batteries and other large-scale energy storages.

3. Conclusion

In summary, we have confirmed that $0.44Na_4Mn_2O_5 \cdot 0.56Na_{0.7}MnO_2$ is a promising cathode for high-energy density NIBs. The cathode exhibits a considerable discharge capacity of 228.0 mAh g^{-1} with an average voltage of ≈2.55 V versus Na$^+$/Na (theoretical energy density is as high as ≈580 Wh kg^{-1}). High areal capacity of ≈1.30 mAh cm^{-2} with high mass loading of 8.19 mg cm^{-2} for sodium storage was achieved. Consequently, the $0.44Na_4Mn_2O_5 \cdot 0.56Na_{0.7}MnO_2$ exhibits high reversible
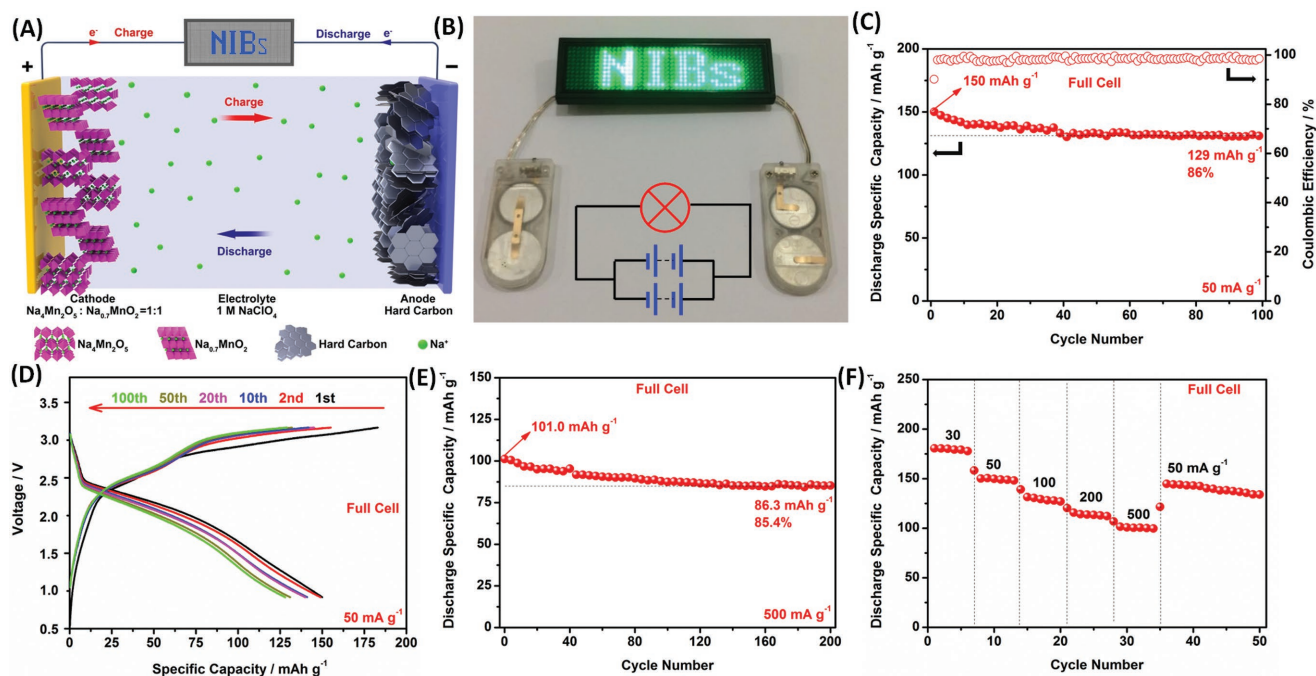
Figure 7. Schematic diagram and electrochemical performance of the Na-ion full batteries based on $0.44Na_4Mn_2O_5 \cdot 0.56Na_{0.7}MnO_2$/hard carbon. A) Schematic diagram of the Na-ion full cell. B) The lighted LED belts driven by the Na-ion full cells. C) Cycling performance and corresponding Coulombic efficiency at 50 mA g^{-1}. D) Charge/discharge curves. E) Cycling performance at 500 mA g^{-1}. F) Rate performance.

discharge capacity and superior cycling stability when tested in Na-ion full cells. Furthermore, on the basis of in situ XRD and electrochemical characterization analysis, we demonstrate that synergistic effect of the composite structured $0.44Na_4Mn_2O_5 \cdot 0.56Na_{0.7}MnO_2$ cathodes are featured with stable crystal skeleton structure and exhibit high reversible capacity during desodiation/sodiation processes. Our work testifies that constructing a synergistic structure to form a new integrated electrode material is an important method to exploit high-energy density and long-life NIBs. Moreover, this work will greatly promote the application of NIBs in the field of large-scale energy storage.

4. Experimental Section

Synthesis of $xNa_4Mn_2O_5 \cdot (1-x)Na_{0.7}MnO_2$: First, $NaNO_3$ (4 mmol), $Mn(CH_3COO)_2$ (2 mmol), and $H_2C_2O_4 \cdot 2H_2O$ (6.0 g) were dispersed in deionized water under constant velocity stirring at room temperature to obtain a light-red solution. Second, the solution was dried at a thermostat, and baked at 180 °C for 12 h to obtain a fluffy solid. Finally, the fluffy solid was sintered in muffle furnace at 300 °C for 0.5 h and then sintered by a tube furnace under flow Ar at 1100 °C for 10 h (4 °C min^{-1}) to obtain $0.44Na_4Mn_2O_5 \cdot 0.56Na_{0.7}MnO_2$. As control experiments, the $0.58Na_4Mn_2O_5 \cdot 0.42Na_{0.7}MnO_2$ and $0.39Na_4Mn_2O_5 \cdot 0.61Na_{0.7}MnO_2$ were synthesized using the same processes, with $NaNO_3$ (6 mmol) and $Mn(CH_3COO)_2$ (2 mmol), and $NaNO_3$ (2 mmol) and $Mn(CH_3COO)_2$ (2 mmol), respectively.

Material Characterization: The as-prepared samples were tested by power XRD on a Bruker D8 Discover X-ray diffractometer equipped with a non-monochromated Cu K X-ray source. The FESEM images were collected using a JEOL-7100F microscopy. EDS was performed using an Oxford EDS IE250. TEM and HRTEM images were recorded using a JEOL JEM-2100F STEM/EDS microscope working at 200 kV. TGA was performed on an STA-449C. Raman spectra and XPS tests were performed using Renishaw INVIA micro-Raman spectroscopy system and VG MultiLab 2000 instrument, respectively.

Electrochemical Measurements: The electrochemical measurements were carried out using 2032 coin cells in a UNIlab Plus Glove Box Workstation filled with pure argon gas. Then, 1 mol L^{-1} $NaClO_4$ in a mixture of ethylene carbon(EC)/dimethyl carbonate(DMC) (2:1 w/w) with 2.5 wt% propylene carbonate (PC) was used as the electrolyte. The cathodes were prepared with 80% $xNa_4Mn_2O_5 \cdot (1-x)Na_{0.7}MnO_2$, 10% acetylene black, and 10% PVDF. The anodes were prepared with 95% hard carbon and 5% polyvinylidene fluoride (PVDF). The cathode and anode were spread on Al and Cu foil, respectively. The mass loading ranges of cathode and anode were controlled to be in a range from 2.51 to 8.19 mg cm^{-2} and 1.9 to 2.4 mg cm^{-2}, respectively. Galvanostatic charge/discharge tests were done using a LAND CT2001A. The test potential ranges were 1.5–4.0 V (cathode) and 0.01–2.0 V (anode) versus Na/Na$^+$, respectively. CV were conducted using CHI600E. Before assembly of Na-ion full batteries, the hard carbon electrode and metal sodium were put together directly, and 3–5 drops of electrolyte was used to cover the hard carbon electrode plate, and kept for 30–50 s. The Na-ion full batteries were performed at a potential range of 0.25–3.25 V versus Na$^+$/Na.

Supporting Information

Supporting Information is available from the Wiley Online Library or from the author.

Conflict of Interest

The authors declare no conflict of interest.

[1] J. Y. Hwang, S. T. Myung, Y. K. Sun, *Chem. Soc. Rev.* **2017**, *46*, 3529.
[2] W. J. Li, C. Han, W. L. Wang, F. Gebert, S. L. Chou, H. K. Liu, X. H. Zhang, S. X. Dou, *Adv. Energy Mater.* **2017**, *7*, 1700274.
[3] N. Yabuuchi, K. Kubota, M. Dahbi, S. Komaba, *Chem. Rev.* **2014**, *114*, 11636.
[4] C. Delmas, *Adv. Energy Mater.* **2018**, *8*, 1703137.
[5] K. Lu, Z. Y. Hu, J. Z. Ma, H. Y. Ma, L. M. Dai, J. T. Zhang, *Nat. Commun.* **2017**, *8*, 527.
[6] K. Lu, B. Song, X. Gao, H. X. Dai, J. T. Zhang, H. Y. Ma, *J. Power Sources* **2016**, *303*, 347.
[7] J. G. Wang, D. D. Jin, R. Zhou, X. Li, X. R. Liu, C. Shen, K. Y. Xie, B. H. Li, F. Y. Kang, B. Q. Wei, *ACS Nano* **2016**, *10*, 6227.
[8] D. Zhou, M. Liu, Q. B. Yun, X. Wang, Y. B. He, B. H. Li, Q. H. Yang, Q. Cai, F. Y. Kang, *Small* **2017**, *13*, 1602015.
[9] J. W. Choi, D. Aurbach, *Nat. Rev. Mater.* **2016**, *1*, 16013.
[10] Y. Li, S. Wang, Y. B. He, L. K. Tang, Y. V. Kaneti, W. Lv, Z. Q. Lin, B. H. Li, Q. H. Yang, F. Y. Kang, *J. Mater. Chem. A* **2017**, *5*, 4359.
[11] T. Von Graberg, *Adv. Energy Mater.* **2018**, *8*, 1703350.
[12] N. Ortizvitoriano, N. E. Drewett, E. Gonzalo, T. Rojo, *Energy Environ. Sci.* **2017**, *10*, 1051.
[13] K. Lu, Z. Y. Hu, Z. H. Xiang, J. Z. Ma, B. Song, J. T. Zhang, H. Y. Ma, *Angew. Chem., Int. Ed.* **2016**, *128*, 10604.
[14] R. J. Clément, P. G. Bruce, C. P. Grey, *J. Electrochem. Soc.* **2015**, *162*, A2589.
[15] J. Billaud, R. J. Clément, A. R. Armstrong, J. Canalesvázquez, P. Rozier, C. P. Grey, P. G. Bruce, *J. Am. Chem. Soc.* **2015**, *46*, 17243.
[16] K. Du, J. Zhu, G. Hu, H. Gao, Y. Li, J. B. Goodenough, *Energy Environ. Sci.* **2016**, *9*, 2575.
[17] Y. Cao, L. Xiao, W. Wang, D. Choi, Z. Nie, J. Yu, L. V. Saraf, Z. Yang, J. Liu, *Adv. Mater.* **2011**, *23*, 3155.
[18] X. Ma, H. Chen, G. Ceder, *J. Electrochem. Soc.* **2011**, *158*, A1307.
[19] D. Su, C. Wang, H. J. Ahn, G. Wang, *Chem. - Eur. J.* **2013**, *19*, 10884.
[20] N. A. Katcho, J. Carrasco, D. Saurel, E. Gonzalo, M. Han, F. Aguesse, T. Rojo, *Adv. Energy Mater.* **2017**, *7*, 1601477.
[21] N. Yabuuchi, M. Kajiyama, J. Iwatate, H. Nishikawa, S. Hitomi, R. Okuyama, R. Usui, Y. Yamada, S. Komaba, *Nat. Mater.* **2012**, *11*, 512.
[22] B. M. D. Boisse, D. Carlier, M. Guignard, C. Delmas, *J. Electrochem. Soc.* **2013**, *160*, A569.

[23] S. Kalluri, K. H. Seng, W. K. Pang, Z. Guo, Z. Chen, H. K. Liu, S. X. Dou, *ACS Appl. Mater. Interfaces* **2014**, *6*, 8953.

[24] C. J. Niu, J. S. Meng, X. P. Wang, C. H. Han, M. Y. Yan, K. N. Zhao, X. M. Xu, W. H. Ren, Y. L. Zhao, L. Xu, Q. J. Zhang, D. Y. Zhao, L. Q. Mai, *Nat. Commun.* **2015**, *6*, 7402.

[25] Y. Liu, Y. Qiao, W. Zhang, H. Xu, Z. Li, Y. Shen, L. Yuan, X. Hu, X. Dai, Y. Huang, *Nano Energy* **2014**, *5*, 97.

[26] Y. L. Zhao, C. H. Han, J. W. Yang, J. Su, X. M. Xu, S. Li, L. Xu, R. P. Fang, H. Jiang, X. D. Zou, B. Song, L. Q. Mai, Q. J. Zhang, *Nano Lett.* **2015**, *15*, 2180.

[27] D. Yuan, X. Hu, J. Qian, P. Feng, F. Wu, R. Mao, X. Ai, H. Yang, Y. Cao, *Electrochim. Acta* **2014**, *116*, 300.

[28] X. P. Wang, X. M. Xu, C. J. Niu, J. S. Meng, M. Huang, X. Liu, Z. A. Liu, L. Q. Mai, *Nano Lett.* **2017**, *17*, 544.

[29] G. Brachtel, R. Hoppe, *Z. Anorg. Allg. Chem.* **1980**, *468*, 130.

[30] M. Freire, N. V. Kosova, C. Jordy, D. Chateigner, O. I. Lebedev, A. Maignan, V. Pralong, *Nat. Mater.* **2016**, *15*, 173.

[31] M. Diazlopez, M. Freire, Y. Joly, C. V. Colin, H. E. Fischer, N. Blanc, N. Boudet, V. Pralong, P. Bordet, *Chem. Mater.* **2018**, *30*, 3060.

[32] S. Guo, P. Liu, H. Yu, Y. Zhu, M. Chen, M. Ishida, H. Zhou, *Angew. Chem., Int. Ed.* **2015**, *127*, 5992.

[33] Y. K. Sun, S. T. Myung, B. C. Park, J. Prakash, I. Belharouak, K. Amine, *Nat. Mater.* **2009**, *8*, 320.

[34] J. Meng, H. Guo, C. Niu, Y. Zhao, L. Xu, Q. Li, L. Mai, *Joule* **2017**, *1*, 522.

[35] J. Y. Hwang, S. M. Oh, S. T. Myung, K. Y. Chung, I. Belharouak, Y. K. Sun, *Nat. Commun.* **2015**, *6*, 6865.

[36] C. J. Niu, X. Liu, J. S. Meng, L. Xu, M. Y. Yan, X. P. Wang, G. B. Zhang, Z. A. Liu, X. Xu, L.Q. Mai, *Nano Energy* **2016**, *27*, 147.

[37] K. B. Kim, J. Das, F. Baier, J. Eckert, *Appl. Phys. Lett.* **2005**, *86*, 3015.

[38] J. S. Meng, C. J. Niu, L. Xu, J. T. Li, X. Liu, X. P. Wang, Y. Z. Wu, X. Xu, W. Y. Chen, Q. Li, Z. Z. Zhu, D. Y. Zhao, L. Q. Mai, *J. Am. Chem. Soc.* **2017**, *139*, 8212.

[39] X. P. Wang, P. Hu, C. J. Niu, J. S. Meng, X. M. Xu, X. J. Wei, C. J. Tang, W. Luo, L. Zhou, Q. Y. An, L. Q. Mai, *Nano Energy* **2017**, *35*, 71.

[40] Y. Wang, J. Liu, B. Lee, R. Qiao, Z. Yang, S. Xu, X. Yu, L. Gu, Y. S. Hu, W. Yang, *Nat. Commun.* **2015**, *6*, 6401.

[41] H. Liu, F. C. Strobridge, O. J. Borkiewicz, K. M. Wiaderek, K. W. Chapman, P. J. Chupas, C. P. Grey, *Science* **2014**, *344*, 1252817.

[42] X. P. Wang, C. J. Niu, J. S. Meng, P. Hu, X. M. Xu, X. J. Wei, L. Zhou, K. N. Zhao, W. Luo, M. Y. Yan, L. Q. Mai, *Adv. Energy Mater.* **2015**, *5*, 1500716.

[43] Q. D. Wang, W. Yang, F. Y. Kang, B. H. Li, *Energy Storage Mater.* **2018**, *14*, 361.

[44] Z. J. Su, C. Yang, B. H. Xie, Z. Y. Lin, Z. X. Zhang, J. P. Liu, B. H. Li, F. Y. Kang, C. P. Wong, *Energy Environ. Sci.* **2014**, *7*, 2652.

[45] S. Xu, Y. Wang, L. Ben, Y. Lyu, N. Song, Z. Yang, Y. Li, L. Mu, H. T. Yang, L. Gu, *Adv. Energy Mater.* **2015**, *5*, 1501156.